nature communications

Article

https://doi.org/10.1038/s41467-025-68046-z

Decoding the gradient-distributed colour centers in electrochromic WO_3

Received: 30 April 2025

Accepted: 16 December 2025

Published online: 14 January 2026

Check for updates

Sikang Xue[1,2,7], Jizhe Cui[3,7], Chuchu Zhou[1,2], Min Shen[1,2], Xiaocong Liang[1,2], Mingyue Wang[1,2], Quanpan Zhao[1,2], Yan Ye[1,2], Kun Xu[4], Yanan Zhao[5], Rongji Jiao[6], Rui-Tao Wen[6], Can Yang[1,2], Zhiyang Yu[1,2] ✉, Rong Yu[3] ✉ & Wandong Xing[1,2] ✉

The optical properties of electrochromic windows can be modulated by embedding electrons and ions simultaneously to realize energy-saving functions. However, the microscopic electrochromic mechanism in cathode materials remains controversial. Herein, we have discovered that the single-crystal WO_3 nanosheets exhibit thickness-dependent electrochromic characteristics. The multislice electron ptychography experiments revealed that the colour centers in electrochromic WO_3 are associated with lattice distortions, and the density of the colour centers decreases from surface to bulk. Moreover, the heterogeneous distribution of polarons induces a phase transition from monoclinic to tetragonal and cubic structures, which in turn causes the band gap of the WO_3 nanosheets to follow a volcano-type trend. This phenomenon elucidates the colour shift of the electrode from yellow to blue or black as the thickness of the nanosheets decreases. By visualizing the actual colour centers of electrochromic materials, our findings provide an optimal framework for the development of high-performance electrochromic devices.

The electrochromic behavior of metal oxides is achieved by applying an electric field, which modulates their optical absorption properties across the ultraviolet–visible-infrared (UV-Vis-IR) spectrum. This technology is instrumental in energy conservation and transparency regulation in applications such as smart windows, aircraft windows, and anti-counterfeiting coatings, etc[1–8]. Despite numerous proposed electrochromic mechanisms for smart materials, such as the classical cathode material WO_3, a universally accepted theory remains elusive[9–13]. In 1973, Deb and colleagues proposed a "colour center" theory to explain the electrochromic mechanism within amorphous WO_{3-x} films. According to this theory, oxygen vacancies (V_O) within the host material create defect energy levels that capture carriers, leading to the absorption of visible light[14]. Since ions can also be injected into host materials during the electrochemical process, charge injection models were developed, and the possibility of charge transit absorption between W^{5+} and W^{6+} species was considered[15,16]. Meanwhile, researchers have discovered that small polarons can form when both ions and electrons are simultaneously incorporated into the crystal structure. They attributed the modulated optical properties of electrochromic materials to the hopping of electrons from W^{5+} to adjacent W^{6+} ions[17–21]. Considering that WO_3 phases can be transformed into tungsten bronze phases with a high concentration of charge carriers upon charge injection, scientists have utilized the Drude model to elucidate that the observed increase in absorption across the visible and infrared spectrum is due to the surface plasmon resonance effect associated with these high-density free carriers[22–29]. However, these

[1]State Key Laboratory of Chemistry for NBC Hazards Protection, College of Chemistry, Fuzhou University, Fuzhou, China. [2]State Key Laboratory of Photocatalysis on Energy and Environment, College of Chemistry, Fuzhou University, Fuzhou, China. [3]MOE Key Laboratory of Advanced Materials, School of Materials Science and Engineering, Tsinghua University, Beijing, China. [4]Department of Mechanical Engineering, Stanford University, Palo Alto, CA, USA. [5]School of Science, Xi'an University of Posts and Telecommunications, Xi'an, China. [6]Department of Materials Science and Engineering, Southern University of Science and Technology, Shenzhen, China. [7]These authors contributed equally: Sikang Xue, Jizhe Cui. ✉e-mail: yuzyemlab@fzu.edu.cn; ryu@tsinghua.edu.cn; xwd@fzu.edu.cn

perspectives fail to offer a clear explanation for the blue-shifted absorption edges observed in the UV-Vis spectra of coloured WO_3.

The inserted electrons and ions affect the density of the free carrier and induce the structural distortion of the host materials to form various phases[30]. For many transition metal compounds, the symmetry of the crystal structures can be influenced by trapping and de-trapping electrons and ions[3,21,31,32]. As revealed by the aberration-corrected transmission electron microscopy, the bond angles and lengths of the host materials can be decreased by embedding ions and electrons under electrochemical environments, thereby promoting the orbitals' overlap between anions and cations[33]. These enhanced hybridizations of the valance electrons within the ion-inserted materials will lower the band gap in the phase, resulting in the red shift of the absorption edge in UV-Vis-IR spectra[34–37]. Monoclinic γ-WO_3 is a stable phase at room temperature, and it can be transformed into orthorhombic, tetragonal, and cubic phases by increasing the qualities of embedded ions and electrons[15]. Note that the symmetry of the phases can be well characterized by the degree of tilting, rotation, and distortion of the corner-sharing [WO_6] octahedra[38]. It is believed that alterations in crystal structures, along with the insertion of electrons and ions, significantly impact the electronic structure of WO_3, which in turn plays a pivotal role in its optical properties[39,40]. Nevertheless, the aforementioned key factors are often neglected, and there remains a lack of atomic-level understanding regarding the spatial distribution of the inserted electrons and ions in coloured WO_3, the identity of the actual colour center, and how the colour center actively modifies optical characteristics. This gap in knowledge constrains the advancement of electrochromic materials and technologies.

Herein, we have chosen γ-WO_3 nanosheets with various thicknesses as a model system to investigate the active mechanism of the colour center. By comparing the crystal structures and optical modulation amplitudes of coloured WO_3 nanosheets of varying thicknesses, the thickness-dependent electrochromic properties of these nanosheets have been revealed. For instance, it has been observed that thinner nanosheets exhibit enhanced electrochromic behavior. By means of state-of-the-art multislice electron ptychography[41,42], the three-dimensional spatial distribution characteristics of the colour center in WO_3 nanosheets have been revealed at the atomic level. By integrating with theoretical calculations, we have bridged the connection between the crystal structure and colour center and found that the colour is tightly related to the density of the colour centers at different depths, from surface to bulk, during the electrochromic process. This work deepens the understanding of the electrochromic process by directly characterizing the atomic structure and depth distribution of the colour center at the microscopic level, offering a solid theoretical foundation for controlling the optical absorption performance of smart materials.

Results and discussion

The macroscopic behaviour in electrochromic WO_3

In our quest to unravel the electrochromic mechanism, we have selected the typical monoclinic γ-WO_3 and compared its macroscopic structures across various states, namely pristine, coloured, and bleached. The highly crystalline WO_3 nanosheets prepared via a hydrothermal process, which were deposited onto the surface of F-doped tin oxide (FTO) electrodes, followed by annealing, exhibit similar-thickness films (Fig. S1) and varying grain thicknesses of 15 ± 6.5, 30 ± 7.4, and 60 ± 12.0 nm (Figs. S2 and S3, details are discussed in Supporting information.). These nanosheets are confined by two basal planes, specifically the {002} planes, and are edged by four-sided facets, comprising two {200} facets and two {020} facets (Fig. S4). As shown in Fig. 1a, a constant negative voltage technique was employed to induce the electrochromic behavior of the WO_3 cathode in a KCl electrolyte within a three-electrode setup. The images of the insets in Fig. 1b demonstrate that the coloured WO_3 electrodes (the detailed experimental conditions were discussed in Figs. S5-S7) undergo a transition from yellow to blue, and ultimately to black, as the grain thickness decreased under the identical experimental conditions. As shown in Fig. 1b, compared with the 30 nm- and 60 nm-thick WO_3 nanosheets, the UV-vis drift reflectance spectrum of the 15 nm-thick WO_3 nanosheets shows maximum reflectance modulation of 96% at wavelengths of 700 nm. In-situ optical transmittance results at 410, 440, and 770 nm reveal that the 15 nm-thick WO_3 nanosheets possess a faster optical response than their thicker counterparts (Fig. S8). These results indicate that the 15 nm-thick WO_3 nanosheets display improved electrochromic properties than other WO_3 nanosheets with a larger thickness. Furthermore, we have calculated the inserted electric charge quantities of the coloured WO_3 with various thicknesses according to the following formula:

$$Q = \int_0^t j^* A \, dt \tag{1}$$

where Q, j, A, and t parameters refer to electric charge, current density, work area, and time. As shown in the J-t plots (Fig. 1c), the 15 nm-thick WO_3 nanosheets accumulate a charge of 1.2 C within 60 s, exceeding that of the 30 nm- and 60 nm-thick counterparts. This indicates that WO_3 nanosheets exhibiting greater light modulation (in the coloured state) accommodate more injected electrons. X-ray photoelectron spectroscopy (XPS) spectra (Fig. S6) and energy-dispersive spectroscopy (EDS) maps (Fig. S7) of the coloured 15 nm-thick WO_3 nanosheets reveal the characteristic signals of K^+ as well as their uniform distribution, demonstrating that the K^+ from the solution could also insert into the WO_3 lattice under applied bias. Inductively coupled plasma (ICP) analysis of coloured K_xWO_3 nanosheets (Fig. 1d) reveals an increase in the K^+ insertion ratio from $13.83 \pm 2.84\%$ to $19.18 \pm 0.36\%$ as the nanosheet thickness decreases from 60 nm to 15 nm. This trend correlates with enhanced optical modulation properties, confirming a positive relationship between K^+ quantity and electrochromic performance. These results indicated that the electrochromic properties of the WO_3 nanosheets are closely linked to the number of inserted electrons and ions. Thinner WO_3 nanosheets can host greater quantities of these species, enhancing their electrochromic performance. Moreover, the optical absorption edge of the coloured K_xWO_3 nanosheets shows an obvious blue shift, while the counterparts of 15 nm thick nanosheets demonstrate a prominent red shift (Fig. 1b). When the coloured K_xWO_3 cathode was exposed to air, which can capture the embedded electrons (briefly termed as the bleached K_xWO_3), the bleaching process was achieved without the need for an additional positive bias potential (Figs. S9-S14), causing the blue cathode to return to pale yellow. This experiment result indicates that the intercalation of electrons is a rate-determining step in achieving the electrochromic behaviour of smart materials.

The X-ray diffraction (XRD) pattern of the pristine WO_3 nanosheets displays a typical monoclinic structure as depicted in Fig.1e. The phase structures of coloured K_xWO_3 nanosheets gradually become tetragonal and cubic as their thicknesses decrease, a phenomenon that is linked to lattice expansion caused by inserted ions and electrons (Fig. S15), which is also evidenced by theoretical simulation in Fig. S16. After de-intercalation of ions and electrons, the XRD patterns of the bleached WO_3 nanosheets with various thicknesses exhibited monoclinic crystal structures. Compared with the Raman spectra of the pristine and bleached WO_3 nanosheets (Fig. 1f), the Raman bands corresponding to the bending mode and stretching variation of W-O-W for the coloured K_xWO_3 nanosheets are weaker, illustrating that the corner-connected W-O-W bonds show stronger rigidity. This is because the bond angle of the corner-connected W-O-W bonds becomes larger to generate more stress and bear the bending or stretching vibration of the chemical bonds. These findings suggested that the embedding of electrons and ions leads to a phase transition and improves the symmetry of the WO_3 nanosheets.

https://doi.org/10.1038/s41467-025-68046-z

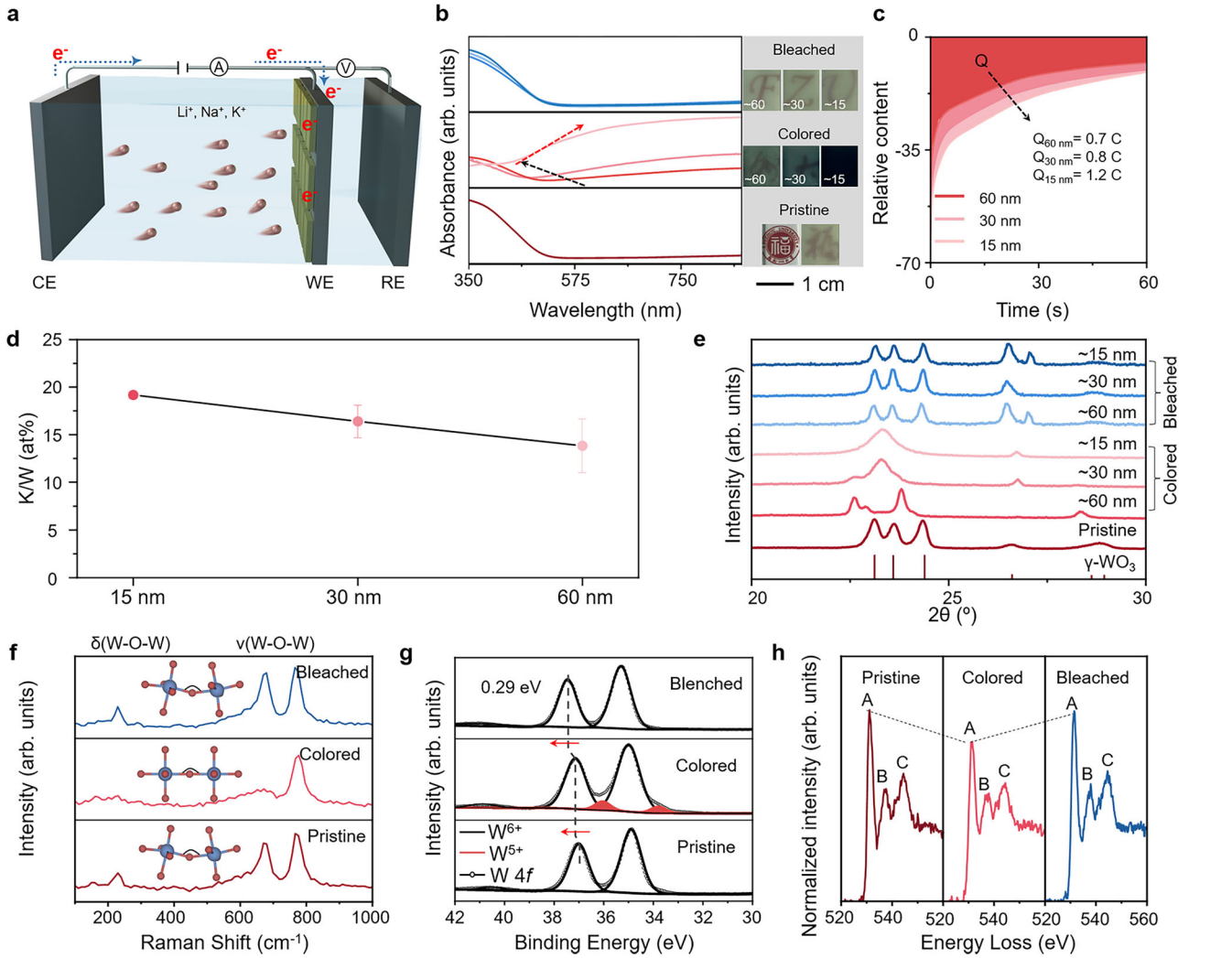

Fig. 1 | Investigation of structure evolution in electrochromic WO_3 nanosheets. **a** A schematic illustration of the electrochromic process showing the electrons and alkali ions injected into the working electrode, where CE, WE, and RE refer to the counter electrode, working electrode, and reference electrode. **b** UV-Vis diffuse reflectance spectroscopy (DRS) of the pristine, coloured, and bleached WO_3 nanosheets with various thicknesses (15 nm, 30 nm, and 60 nm) and their corresponding photograph in the insets of **b**, demonstrating that thinner nanosheets exhibit darker colour. **c** Chronoamperometry plots of coloured WO_3 nanosheets with different thicknesses, showing that more electrons were injected into the thinner nanosheets. **d** The inductively coupled plasma (ICP) curves of the different WO_3 nanosheets, showcasing that the content of K^+ ions in electrodes is negatively correlated to the thickness of the WO_3 nanosheets. The error bar represents the standard deviation, calculated from three repeated experiments. **e** XRD patterns of the pristine, coloured, and bleached WO_3 nanosheets with different thicknesses, displaying that the nanosheets of ~15 nm thick, which possess the highest electrochromic performance, undergo a distinct phase transition from monoclinic to cubic and then back to monoclinic during the electrochromic and fading processes. **f**. Raman spectra of the pristine, coloured, and bleached WO_3 nanosheets, demonstrating that the absorption band of the bending mode (200–400 cm^{-1}) and stretching vibration (600–740 cm^{-1}) for the W-O-W bonds is weakened at the coloured state, and indicating that the bond angle of the W-O-W bonds is enlarged after electrochromic. The blue and pink balls represent to W atoms and O atoms, respectively. **g** XPS spectra of the WO_3 nanosheets at various states, showing that W^{5+} species appeared at the coloured state. **h** Electron-energy loss spectra of the pristine, coloured, and bleached WO_3 nanosheets at O *K*-edges. The apparent suppression of the A peak in the coloured state suggests that electrons were injected into W 5*d* orbitals.

From the XPS spectra of the WO_3 nanosheets at various states (Fig. 1g), we found that the high-resolution W 4*f* spectrum of the coloured K_xWO_3 nanosheets reveals the presence of the W^{5+} groups at 36.1 eV and 33.7 eV, along with a blue shift in the W^{6+} species at 37.1 eV and 35.0 eV. Concurrently, the bleached K_xWO_3 nanosheets no longer exhibit the W^{5+} groups, indicating that the electrochromic behaviour is intimately connected to inserted electrons within the cathode system. Regarding the electronic structure, it is delineated by the changes observed in the O *K* edge through electron-energy loss spectroscopy. The electron transition from the O 1*s* orbitals to the hybridized orbitals between O 2*p* and W 5*d*/6*sp* orbitals accounts for the three distinct peaks (labeled A, B, and C) in the O *K*-edge spectrum, as depicted in Fig. 1h. The coloured K_xWO_3 samples exhibit reduced signal intensity from the A peaks, attributed to the insertion of electrons into the W 5*d* orbitals. Conversely, the bleached K_xWO_3 nanosheets, which lack the additional electrons, show a recovery in the intensity of the A peaks to levels comparable to those of the pristine WO_3 samples[43]. In light of the aforementioned experimental findings, it is determined that the coupled doping of ions and electrons can modulate the crystal structures and electronic structures of WO_3, forming the colour center that will enable the cathode's electrochromic properties.

Three-dimensional visualization of the spatial distribution of colour centers

To identify the spatial distribution of the colour centers at the atomic scale, we employed multislice electron ptychography to characterize

https://doi.org/10.1038/s41467-025-68046-z

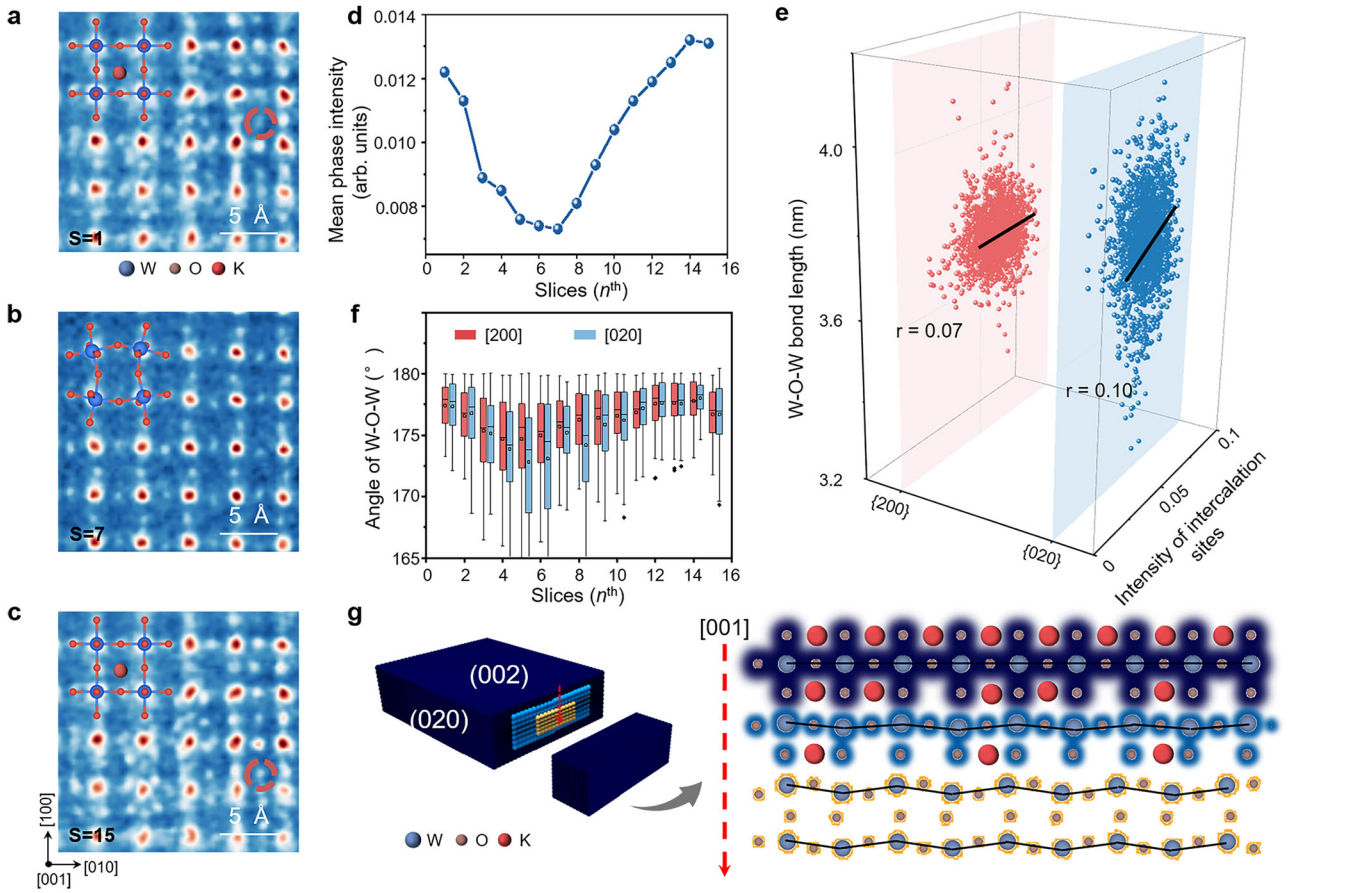

Fig. 2 | Multislice electron ptychography characterisation of the coloured K_xWO_3 nanosheets. a–c Enlarged and identical phase images of the coloured K_xWO_3 nanosheets with a thickness of 15 nm at 1 nm, 7 nm, and 15 nm in depth (slice 1 is defined as 1 nm in thickness from the top surface), showing that K^+ ions are inserted into the A position of pseudo-K_xWO_3 perovskite, as boxed by red circles. **d** The mean phase intensity of the K^+ intensity distribution from slices 1 to 15. **e** The Pearson correlation coefficients of the interplanar spacing of the {200 and {020} facets from slices 1 to 15 as a function of the intensity of K^+ ions, showcasing that the more K^+ ions, the more obvious lattice distortion. **f** The statistical box diagrams of the changed W-O-W chemical bonds at every slice in coloured K_xWO_3 nanosheets in 3 replicates, showing that the bond angle rises with area proximity to the surface along [200] and [020] zone axes, respectively. **g** Schematic view of the three-dimensional distribution of the colour centres in K_xWO_3 nanosheets, showcasing that the monoclinic structure (yellow atoms) gradually transforms into tetragonal (light blue atoms) and ultimately cubic structures (dark blue atoms) from the bulk to the surface, driven by embedded K^+ ions along the [001] direction, thereby exhibiting pronounced depth-dependent lattice distortion.

the electrochromic K_xWO_3 nanosheets that were treated under a bias potential of -1 V. This technique is a coherent diffraction imaging method with high spatial resolution, phase accuracy, dose efficiency, and depth resolution in the direction of electron beam propagation[44–47]. For a 15 nm-thick coloured K_xWO_3 nanosheet, 15 object slices of 1 nm thick were used for ptychography reconstructions. The depth-dependent ptychographic phase images of the coloured K_xWO_3 nanosheet are shown in Fig. S17. The magnified and corresponding regions of surface slices 1 and 15 (Fig. 2a-c) reveal that K^+ ions were intercalated at the A positions within the pseudocubic structures, as indicated by the red circles, while the central slice 7 displays a scarcity of interstitial K^+ ions (Figs. S18-S20). Furthermore, the mean phase intensity (Fig. 2d) and the frequency histograms (Fig. S21) for K^+ intensity distribution within each slice form a parabola with an upward opening, indicating a higher concentration of interstitial K^+ ions near the surface region compared to the bulk area. This confirms that K^+ ions, along with electrons, initiate from the surface regions. Additionally, these results demonstrate that the depth of the inserted K^+ ions is ~ 3 nm.

Then, the interplanar spacing (a and b) of the {200} and {020} facets (i.e., the bond length of adjacent W atoms, including horizontal and vertical) from slices 1 to 15 were quantitatively described by the atomic positions of W and O atoms determined through Gaussian fitting (Fig. S22). Note that the local lattice spacings are increased to 3.9 Å compared with pristine monoclinic WO_3 of 3.7 Å. Furthermore, the Pearson correlation coefficient values for a and b are 0.07 and 0.10 (Fig. 2e), respectively, indicating that the lattice expansion occurs both in the {200} and {020} planes, which is attributed to the insertion of K^+ ions and electrons and positively correlated with the embedded K^+ ions concentration.

As seen from Fig. 2f, when the depth of doped K^+ ions is close to the top and bottom surfaces, the W-O-W bond angles become larger along the [200] and [020] directions, and the part of W-O-W angles tend to even rise to 180° among the slices near the surface for producing the cubic K_xWO_3 and cubic WO_3 crystal units. This phenomenon was also observed in the Na_xWO_3 nanosheets (Fig. S23). These findings show that the injected ions and electrons can cause the lattice distortion of the [WO_6] octahedrons, which triggers the phase transition of the WO_3 nanosheets. As mentioned in the review literature[21], when the alkali metal ions and electrons are injected into the host materials WO_3, they are believed to form the localized small polarons and induce lattice distortions around the trapping sites. As shown in the schematic diagram (Fig. 2g), limited by the charge transfer dynamics, K^+ ions in the WO_3 nanosheets exhibit gradient distribution

https://doi.org/10.1038/s41467-025-68046-z

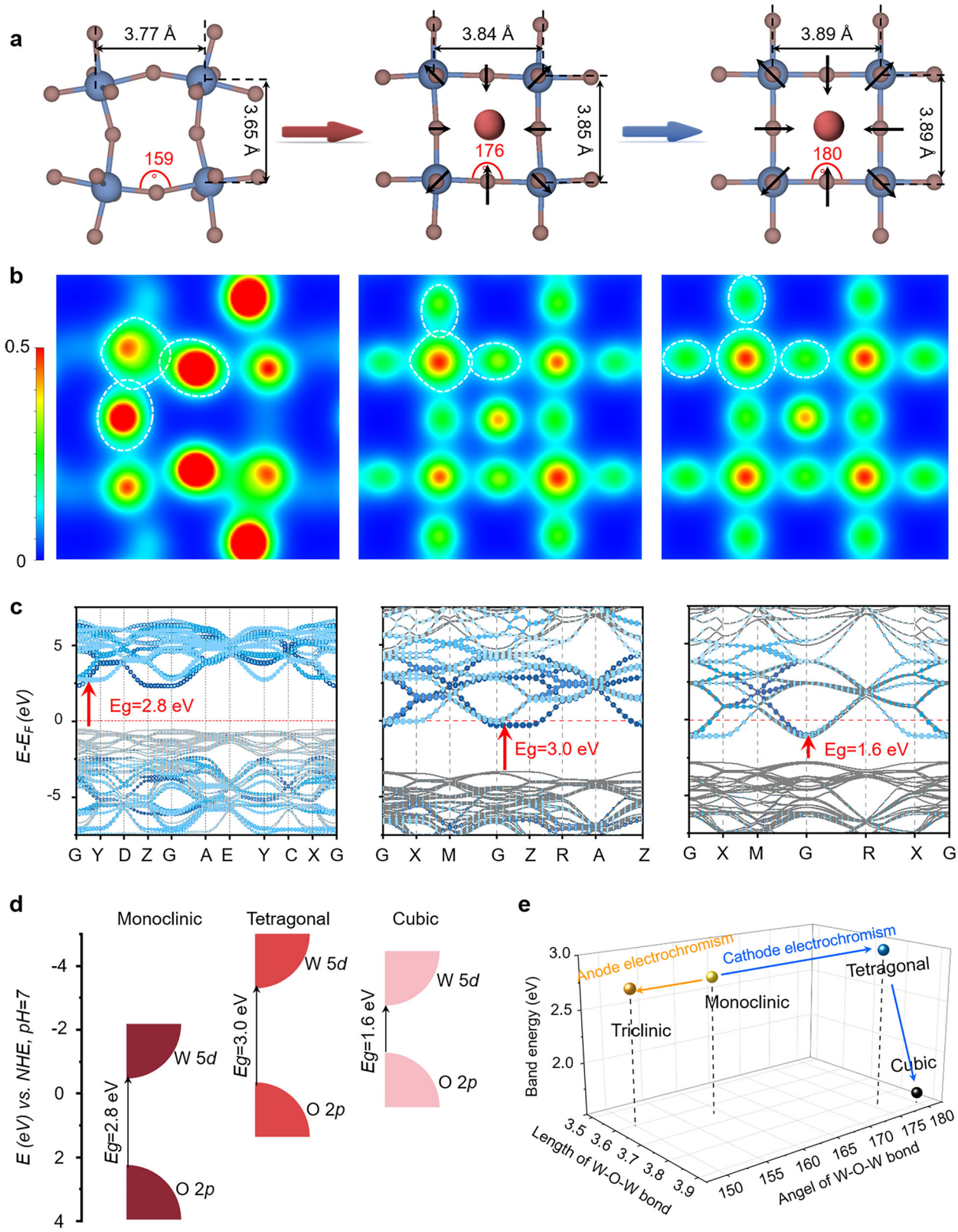

from the inside outward as companies with gradually disappearing zigzag lattice distortion, causing depth-dependent lattice distortion (monoclinic, tetragonal, and cubic) from bulk to surface. The results show that the higher amounts of K^+ ions and electrons embedded, the greater the lattice distortion, which is conducive to forming different colour centers (yellow, blue, and black) for modulating the macroscopic colour of the working electrode.

Analysis of the electrochromic mechanism

To reveal the electrochromic mechanism, the effect of the lattice distortions on the changes in electronic structures after inserting ions and electrons was investigated. Figure 3a shows the relaxed structure units of the γ-WO_3 (left panel, monoclinic), $K_{0.125}WO_3$ with an additional 0.125 *e*/unit cell (middle panel, tetragonal), and $K_{0.25}WO_3$ with an additional 0.25 *e*/unit cell (right panel, cubic) by employing density

Fig. 3 | Electronic structures of the coloured K_xWO_3 nanosheets with lattice distortion. a Relaxed atomic structure along [001] direction of the monoclinic WO_3 (left panel), tetragonal $K_{0.125}WO_3$ with additional 0.125 *e*/unit cell (middle panel), and cubic $K_{0.25}WO_3$ with additional 0.125 *e*/unit cell (right panel). The blue, khaki, and red atoms refer to the W, O, and K atoms. The W-O-W bond lengths and angles in corner-sharing-connected [WO_6] octahedra are labelled in **a**, displaying the zigzag distortion of W-O-W bonds. **b** Two-dimensional (2D) charge density maps (q/Å^2) of the three structures in **a**, showcasing that the orbital overlap areas between W and O atoms have been reduced after embedding more ions and electrons. **c** The band structures of the monoclinic WO_3 (left panel), tetragonal $K_{0.125}WO_3$ with additional 0.125 *e*/unit cell (middle panel), and cubic $K_{0.25}WO_3$ with additional 0.125 *e*/unit cell (right panel). **d** Band structures of these samples from theory calculations and K-M plots, demonstrating that their corresponding band gaps are higher and lower than the monoclinic WO_3 crystal counterparts. **e** The relationship plot between the photograph colour of electrochromic materials and their lattice distortion, showing that the cathode electrochromic responds to the increased band gap, while the anode electrochromic exhibits decreased band gap for WO_3 nanosheets.

functional theory (DFT), exhibiting the significant structural expansion and obvious lattice distortion. Note that the intercalations of more electrons and K^+ ions do not change the connected and rotated pattern of the corner-sharing [WO_6] octahedrons but increase the W-O-W bond angles and bond length to 180° and 3.89 Å, respectively. This result indicates that the cooperative interaction of injected electrons and K^+ ions at interstitial sites offers strong stress to relax the zigzag deformation of O atoms along [100], [010], and [001] directions in multiple areas of the samples. Predictably, the synergistic effect is the reason that the XRD patterns of coloured K_xWO_3 samples with different thicknesses (30 nm and 15 nm) gradually become tetragonal and cubic symmetry as the thickness decreases (Fig. 1e). Additionally, due to the distinct expansion of the W-O-W bond angles and bond length, the orbital overlap of W 5*d* and O 2*p* in the 2D charge density maps gradually reduced from the monoclinic WO_3 to tetragonal $K_{0.125}WO_3$ and cubic $K_{0.25}WO_3$ (Fig. 3b). This will have a significant effect on the band structure of the coloured K_xWO_3 nanosheets. As from the Kubelka-Munk plots (Fig. S24) and calculated band structures (Fig. 3c) of the cathode electrochromic samples, the band gap of the 30 nm-thick coloured K_xWO_3 nanosheets with tetragonal symmetry is 3.0 eV (Fig. 3d), which is larger than that of the pristine WO_3 nanosheets (2.8 eV). This is the cause of the blue shift of the adsorption edge in diffuse reflectance spectroscopy (DRS) spectra of 30 nm-thick tetragonal K_xWO_3 nanosheets (Fig. 1b), thereby resulting in the yellow WO_3 electrode changing to blue. Furthermore, the band gap of the 15 nm-thick cubic K_xWO_3 sample is reduced to 1.6 eV (Fig. 3c and Fig. S25). This changed electronic structure gives rise to the redshift in DRS spectra of cubic K_xWO_3 nanosheets, making the WO_3 cathode black. Accordingly, these local atomic structures with different degrees of distortion induced by various concentrations of polarons are the real colour centers of electrochromic WO_3 nanosheets. Therefore, relatively few embedded K^+ ions and electrons can only induce the slight lattice distortion of the 60 nm-thick WO_3 nanosheets, suppressing the improvement of optical modulation amplitude performances (Fig. 1). Inspired by the above results, we forecasted that the anode electrochromic of the WO_3 nanosheets, elevating the orbital overlap areas, could be a feasible means to obtain red nanosheets (Fig. 3e). However, the experimental results show that although the triclinic WO_3 nanosheets have the reduced W-O-W bond angles and band gap (2.78 eV), they exhibit a negligible red-shift of adsorption edge because the W^{6+} cannot be further deeply oxidized (Fig. S26).

The connection between embedded ion sizes and colour centers

We have also discussed the diffusion behaviour of the embedded ions from the surface toward the bulk during the electrochromic process within WO_3 nanosheets. For the γ-WO_3 nanosheets, the diffusion pathway of embedded ions is preferred for transporting along the [001] directions (Figs. S27-S31). As depicted in the inset of Fig. 4a, the slab model of K^+ ions penetrated the three layers of WO_3 nanosheets, as viewed from the side, has been built to mimic the migratory routes from the surface to bulk. The calculation results show the diffusion barrier rises to 16.8 eV as the K^+ ion penetration layers go deeper by utilizing the climbing image nudged elastic band (CI-NEB) method[48], implying that plentiful K^+ ions inclined to coordinate on the surface region of the WO_3 electrode (Fig. 4a). Although the faster embedding of electrons can promote the inserting of K^+ ions, there are still very few K^+ ions that can overcome the diffusion barrier to migrate into the depths of the bulk, producing a specific intercalation depth for the embedded ions as revealed by electron microscopy. This finding suggests that the method to improve the optical modulation amplitude of work electrodes is to decrease the size of the embedded ions, increase the pore size of the host materials, and reduce the thickness of the work electrodes to lower the diffusion barrier.

To facilitate the lattice distortion behaviour of the host materials, the electrolyte with smaller radius ions to replace the K^+ ions, such as H^+, Li^+, and Na^+ ions, was employed, respectively. We found that the colour of the WO_3 nanosheets inserted with H^+, Li^+, and Na^+ also displays blue and black (Fig. S32), and the DRS spectra of the 15 nm-thick H_xWO_3 nanosheets, inserted with more ions and electrons, show the most obvious optical modulation amplitude properties among these ion-inserted WO_3 samples at the wavelength of 700 nm (Fig. S33). As shown in Fig. 4b, the 60 nm-thick H_xWO_3 nanosheets show cubic structures, while the 60 nm-thick Li^+ and Na^+-inserted WO_3 nanosheets exhibit tetragonal structures, indicating that H^+ ions with smaller sizes were easily inserted into the WO_3 nanosheets to trigger obvious lattice distortion. Meanwhile, plentiful embedded ions and electrons can produce high-density polarons, which can expand the W-O-W bond angle and length of the H_xWO_3 nanosheets (Fig. 4c) to 3.9 Å and 180° for reducing the band gap to 1.6 eV (Fig. S34). These prominent lattice distortions were also resolved in the 15 nm-thick coloured Li_xWO_3 and Na_xWO_3 electrodes (Fig. 4c, Figs. S35 and S36). These results demonstrate that the colour of the WO_3 nanosheets is unrelated to the ion types, but is closely correlated with the degree and range of lattice distortion, which is positive to the qualities of the embedded ions and electrons (Fig. 4d).

Ion-insertion materials with coupled ion-electron transfer processes have been widely applied to store electrons and modulate the optical properties in batteries, catalysis, electrochromic, etc. However, the coupling mechanism between the host and guest (ions and electrons) regarding the electronic structures of the host materials remains ambiguous due to the ion-electron-insertion host materials' complicated crystal and unseen ion-electron transport dynamics. This work has revealed that the colour centre of the classical electrochromic materials γ-WO_3 originated from the ion-electron-induced lattice distortion, manipulating the band structures of the host materials for achieving the modulation of the optical properties. Meanwhile, the density of the colour centre would also grow by improving the quantity of the injected ions and electrons, producing a more noticeable optical modulation amplitude. These findings pave the way for the structural design of electrochromic materials, semiconductor devices, energy storage materials, functional materials with broad-spectrum absorption, etc.

In summary, taking WO_3 nanosheets as an example, we have revealed the thickness-dependent electrochromic performances of coloured K_xWO_3 and clarified that the lattice distortion of the corner-sharing [WO_6] octahedra, transitioning from the monoclinic to the tetragonal and cubic phases, is responsible for the colour center of the cathode electrochromic materials. The results of the multislice

https://doi.org/10.1038/s41467-025-68046-z

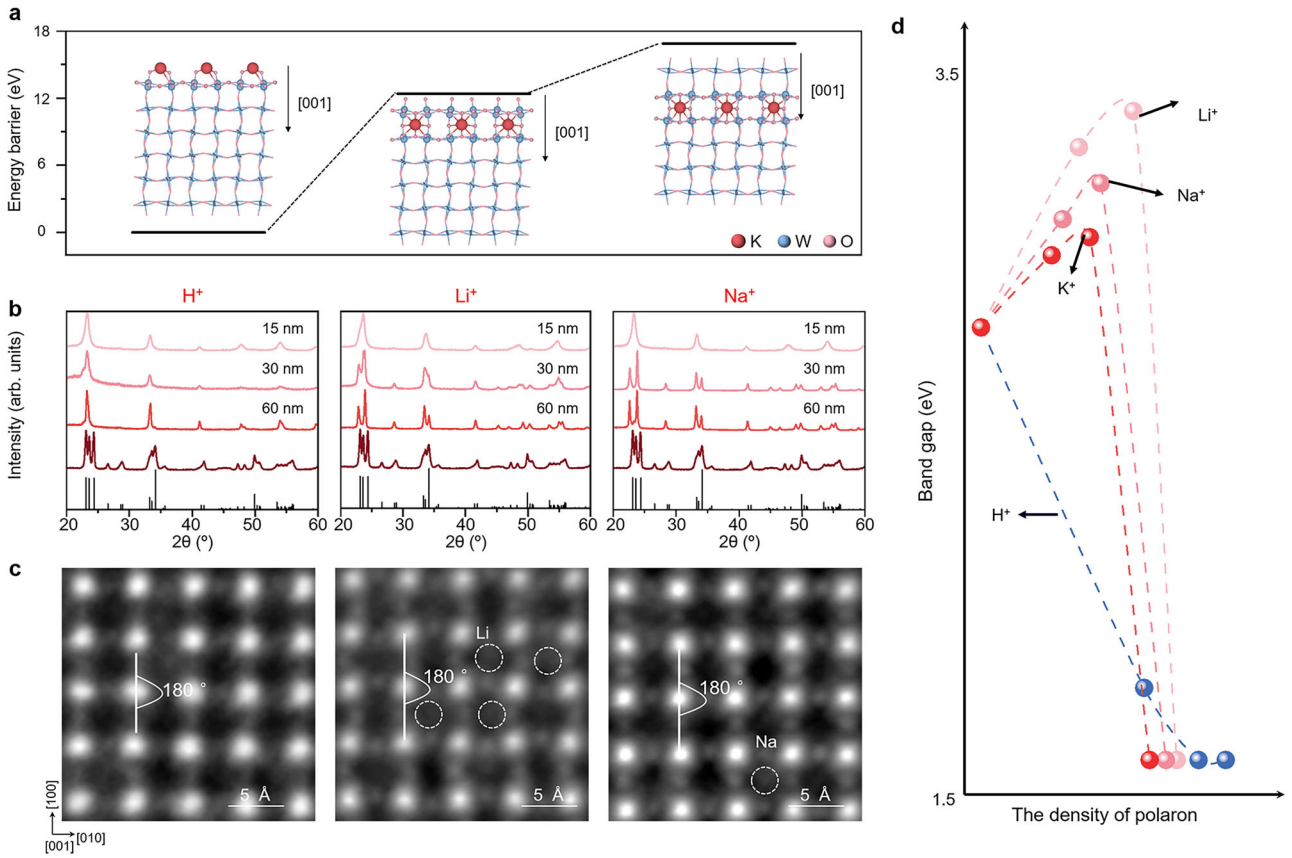

Fig. 4 | The lattice distortion of WO_3 nanosheets under various electrolytes. **a** Transport energy barrier of the embedded K^+ ions across the different layers of WO_3 nanosheets from surface to subsurface to bulk, showing that the transport energy would rapidly rise when K^+ ions are inserted into the first and second layers. **b** XRD patterns of the coloured WO_3 with various thicknesses embedded with H^+ (left panel), Li^+ (middle panel), and Na^+ (right panel) ions, displaying that thinner nanosheets inserted with smaller anode ions produce more radical phase transitions. **c** iDPC images of the coloured H_xWO_3 (left panel), Li_xWO_3 (middle panel), and Na_xWO_3 (right panel) nanosheets with a thickness of 15 nm, demonstrating that the embedded H^+, Li^+, and Na^+ ions (as revealed by red circles) induce the lattice distortion of the corner-sharing connected WO_3 structures to form polarons, respectively. **d** Effect of the radius of ions on the crystal symmetry and band gap, showing that the symmetry-dependent band gap is reduced under the electrolyte with smaller anode ions.

electron ptychography experiments show that the concentration of polarons increases from the bulk to the surface. This is because the inserted electrons and ions show a gradually decreasing distribution from the surface to the bulk. In addition, the band gap of the pristine WO_3 electrodes can be enlarged by the formation of the tetragonal phase, which occurs through slight structural relaxation, and can be reduced by severe lattice distortion in the cubic phase. This leads to a gradient change in the macroscopic colour, ranging from yellow to blue and then to black. Furthermore, the degree and extent of the lattice distortion are positively correlated with the amount of the embedded ions and electrons. This work demonstrates that the structure-dependent optical adsorption properties can be precisely controlled by modulating the degree of lattice distortion, offering a theoretical basis for the structural design of high-performance electrochromic materials, photocatalytic materials, electrode materials, etc.

Methods

Preparation of WO_3 nanosheets with a thickness of 15 nm

The WO_3 nanosheets with a thickness of 15 nm were synthesized by a chemical bath deposition method. 1 mmol $Na_2WO_4{\cdot}2H_2O$ and 1 mmol oxalic acid were added into 55 mL of nitric acid solution containing 5 mL concentrated nitric acid. After 1 h of agitation, the above suspension was transferred to a bottle with a blue cover and kept at 60 °C for 8 h. Then, the products were collected via countrifying by ethanol and water several times and dried overnight.

Preparation of WO_3 nanosheets with a thickness of 30 nm

The WO_3 nanosheets with 30 nm thick were obtained by a hydrothermal method. 1 mmol $Na_2WO_4{\cdot}2H_2O$, and 1.5 mmol citric acid were sequentially added into 33 mL hydrochloric acid solution with the concentrations of 6 M under agitation. After 30 minutes of stirring, the above suspension was transferred to a polytetrafluoroethylene reactor with a volume of 50 mL. Then, the reactor was sealed with the stainless-steel outer lining and heated at 120 °C for 24 h. The sample was centrifuged by ethanol and water several times after cooling down to room temperature and dried at 60 °C for 12 h.

Preparation of WO_3 nanosheets with a thickness of 60 nm

The WO_3 nanosheets with a thickness of 60 nm were fabricated via a hydrothermal method according to our previous study[39,49]. 1.6 mL concentrated hydrochloric acid was dropped into the mixture of 1 mmol $Na_2WO_4{\cdot}2H_2O$, 1.5 mmol citric acid, 5 mmol glucose, and 60 mL H_2O. The mixed solution was stirred for 30 min. The above suspension was then poured into a sealed stainless-steel autoclave for hydrothermal treatment at 160 °C for 8 h. After cooling naturally, the product was collected after washing by in order of water and ethanol and drying for overnight.

Characterizations

The optical properties of the as-prepared samples were studied by UV-Vis diffuse reflectance system spectrometry (UV-Vis DRS, Varian Cary 500). The phase structures of the WO_3 nanosheets were investigated

by powder X-ray diffraction analysis with Cu Kα1 radiation (λ = 1.5406 Å), and Raman spectroscopy (Invia Reflex equipment with excitation light wavelength of 325 nm) was employed to observe the stretching vibration of the W-O-W bond. XPS measurements (Brand: Thermo ESCALAB250 outfitted with a monochromatized Al Kα line source) were applied to detect the surface chemical states of the pristine, colored, and bleached 15 nm-thick WO_3 nanosheets without etch, which can change the raw crystal structures of the WO_3-based samples. The morphologies of as-prepared WO_3 nanosheets were measured by scanning electron microscopy (SEM, Helios G4). The 4D datasets were collected by a probe aberration-corrected transmission electron microscopy (AC-TEM, FEI Titan Cubed Themis G2 operated at 300 kV with a pixel array detector EMPAD), while iDPC images and EELS analysis in scan transmission electron microscopy (STEM) mode were obtained to visualize the changes in crystal structures for the pristine, colored, and bleached WO_3 nanosheets with various thicknesses. The electrochromic experiments were completed by a three-electrode system (BAS Epsilon electrochemical system), where WO_3 nanosheets drop-casted onto the F-doped tin oxide (FTO) substrate were applied as the working electrode, the Pt electrode was used as the counter electrode, and the Ag/AgCl electrode, in 3.0 M KCl electrolyte solution, was used as the reference electrode. Before preparing the working electrode on FTO, the FTO glasses were cleaned with ethanol and acetone solutions several times, respectively, and then dried at 60 °C. Subsequently, the samples of 2 mg were dispersed in 1 mL of ethanol under ultrasound to obtain a suspension. The suspension was dropped onto a fixed area of the FTO substrate. After drying naturally, the FTO glasses with samples were heated at 400 °C for 2 h to improve the interfacial contact between the FTO glasses and samples. For the electrochemical measurements, the electronic impedance spectroscopy (EIS) curves of the as-constructed samples were performed at the region of 200 kHz–50 mHz with Nyquist plots, and cyclic voltammetry (CV) curves were also measured in the region of -1.5-1.5 V on the BAS Epsilon electrochemical workstation. In situ optical transmittance spectra were recorded in real-time by a fiber-optical instrument from Ocean Optics (QEpro, Ocean Optics, USA). The effective optical range was from 350 nm to 1600 nm. Electrochemical measurements were carried out on a CHI660e electrochemical workstation from CHI, CH Instruments Inc., USA.

Details of multislice electron ptychography

The acquisition conditions for the 4D data used in ptychography were set with an underfocus of 20 nm, a scan step size of 0.37 Å, a screen current of 15 pA, and a dwell time of 0.5 ms for each scan point. For the acquired 4D data, we utilized the adaptive propagator ptychography method (APP) proposed by Sha et al.[44]. to reconstruct the object. In this process, 5 mixed states for the electron probe were chosen, and each 128 × 128 diffraction pattern was expanded to 200 × 200 in order to obtain a more refined object function.

Details of the calculations and electrical simulations

All calculations were completed using the DFT calculations implemented in the Vienna ab initio simulation package (VASP, version 5.4.4)[50,51] with the Projector Augmented Wave method[52]. The Perdew–Burke–Ernzerhof was used to describe the function of the exchange-correlation term[53]. The hybrid Heyd-Scuseria-Enrzerhof (HSE06) approximation to the exchange-correlation functional was used for calculating the electronic structures. The plane wave-off cutoff energy was set at 520 eV. The DFT-D3 correction method was used to describe the van der Waals interaction[54]. Convergence criteria of energy and force for all geometry structures were fixed to 10^{-5} eV $atom^{-1}$ and 0.01 eV $Å^{-1}$. The k-points were generated using the Monkhorst-Pack mesh[55]. For the slab model, a vacuum space was fixed as 16 Å along the z direction to minimize the interface between surface slabs.

Data availability

Additional data supporting the findings of this study are reported in the Supplementary Information. Any additional data are available from the corresponding author upon request. The source data are available in this paper. Source data are provided with this paper.

References

1. Lu, N. et al. Electric-field control of tri-state phase transformation with a selective dual-ion switch. *Nature* **546**, 124–128 (2017).
2. Wen, R.-T. et al. Eliminating degradation and uncovering ion-trapping dynamics in electrochromic WO_3 thin films. *Nat. Mater.* **14**, 996–1001 (2015).
3. Zhang, R. et al. Capturing ion trapping and de-trapping dynamics in electrochromic thin films. *Nat. Commun.* **15**, 2294 (2024).
4. Chou, H.-H. et al. A chameleon-inspired stretchable electronic skin with interactive colour changing controlled by tactile sensing. *Nat. Commun.* **6**, 8011 (2015).
5. Wang, J. et al. Large area co-assembly of nanowires for flexible transparent smart windows. *J. Am. Chem. Soc.* **139**, 9921–9926 (2017).
6. Wang, B. et al. A facile strategy to construct Au@V_xO_{2x+1} nanoflowers as a multicolour electrochromic material for adaptive camouflage. *Nano Lett* **22**, 3713–3720 (2022).
7. Li, X. et al. Solution-processable electrochromic materials and devices: roadblocks and strategies towards large-scale applications. *J. Mater. Chem. C* **7**, 12761–12789 (2019).
8. Fan, Q. et al. Dynamic thermoregulatory textiles woven from scalable-manufactured radiative electrochromic fibers. *Adv. Funct. Mater.* **34**, 2310858 (2024).
9. Liu, J.-W. & Yu, S.-H. Emergent motifs of macroscopic nanowire assemblies. *Nat. Sci. Rev.* **2**, 392–393 (2015).
10. Cheng, W. et al. Photodeposited amorphous oxide films for electrochromic windows. *Chem* **4**, 821–832 (2018).
11. Doshi, S. et al. Electrochemically mutable soft metasurfaces. *Nat. Mater.* **24**, 205–211 (2025).
12. Guo, J. et al. Fast-switching WO_3-based electrochromic devices: design, fabrication, and applications. *Acc. Mater. Res.* **4**, 438–447 (2023).
13. Shao, Z. et al. Tri-band electrochromic smart window for energy savings in buildings. *Nat. Sustain.* **7**, 796–803 (2024).
14. Deb, S. K. Optical and photoelectric properties and colour centres in thin films of tungsten oxide. *Philos. Mag.* **27**, 801–822 (1973).
15. Luo, Z. et al. Revealing the charge storage mechanism of nickel oxide electrochromic supercapacitors. *ACS Appl. Mater. Interfaces* **12**, 39098–39107 (2020).
16. Hersh, H. et al. Mechanism of electrochromism in WO_3. *Appl. Phys. Lett.* **27**, 646–648 (1975).
17. Hashimoto, S. & Matsuoka, H. Mechanism of electrochromism for amorphous WO_3 thin films. *J. Appl. Phys.* **69**, 933–937 (1991).
18. Mattox, T. M. et al. Influence of shape on the surface plasmon resonance of tungsten bronze nanocrystals. *Chem. Mater.* **26**, 1779–1784 (2014).
19. Yue, X. et al. Real-time observation of the buildup of polaron in α-$FAPbI_3$. *Nat. Commun.* **14**, 917 (2023).
20. Zhao, D. et al. Copper intercalation induces amorphization of 2D Cu/WO_3 for room-temperature ferromagnetism. *Angew. Chem. Int. Ed.* **136**, e202412811 (2024).
21. Franchini, C. et al. Polarons in materials. *Nat. Rev. Mater.* **6**, 560–586 (2021).
22. Zhang, H. et al. Highly mobile large polarons in black phase $CsPbI_3$. *ACS Energy Lett* **6**, 568–573 (2021).
23. Saenger, M. et al. Polaron and phonon properties in proton intercalated amorphous tungsten oxide thin films. *Phys. Rev. B.* **78**, 245205 (2008).

24. Plankl, M. et al. Subcycle contact-free nanoscopy of ultrafast interlayer transport in atomically thin heterostructures. *Nat. Photonics* **15**, 594–600 (2021).
25. Sood, A. et al. Electrochemical ion insertion from the atomic to the device scale. *Nat. Rev. Mater.* **6**, 847–867 (2021).
26. Besnardiere, J. et al. Structure and electrochromism of two-dimensional octahedral molecular sieve h'-WO_3. *Nat. Commun.* **10**, 327 (2019).
27. Li, K. et al. Lattice-contraction triggered synchronous electrochromic actuator. *Nat. Commun.* **9**, 4798 (2018).
28. Tegg, L. et al. Bulk scale fabrication of sodium tungsten bronze nanoparticles for applications in plasmonics. *Nanotechnology* **29**, 40LT02 (2018).
29. Agrawal, A. et al. Localized surface plasmon resonance in semiconductor nanocrystals. *Chem. Rev.* **118**, 3121–3207 (2018).
30. Tong, C. et al. Synergy between ion migration and charge carrier recombination in metal-halide perovskites. *J. Am. Chem. Soc.* **142**, 3060–3068 (2020).
31. He, Y. et al. Atomistic conversion reaction mechanism of WO_3 in secondary ion batteries of Li, Na, and Ca. *Angew. Chem. Int. Ed.* **55**, 6244–6247 (2016).
32. Prusty, G. et al. Ultrathin plasmonic tungsten oxide quantum wells with controllable free carrier densities. *J. Am. Chem. Soc.* **142**, 5938–5942 (2020).
33. Gao, L. et al. Unveiling strong ion-electron-lattice coupling and electronic antidoping in hydrogenated perovskite nickelate. *Adv. Mater.* **35**, 2300617 (2023).
34. Magnéli, A. Tungsten bronzes containing six-membered rings of WO_6 octahedra. *Nature* **169**, 791–792 (1952).
35. Ikeuchi, Y. et al. High-pressure synthesis of fully occupied tetragonal and cubic tungsten bronze oxides. *Angew. Chem. Int. Ed.* **129**, 5864–5867 (2017).
36. Zheng, H. et al. Nanostructured tungsten oxide-properties, synthesis, and applications. *Adv. Funct. Mater.* **21**, 2175–2196 (2011).
37. Wang, W. et al. Phase transformations upon doping in WO_3. *J. Chem. Phys.* **146**, 214504 (2017).
38. Liu, S. et al. Perovskite smart windows: the light manipulator in energy-efficient buildings. *Adv. Mater.* **36**, 2306423 (2024).
39. Xue, S. et al. Enriching surface-ordered defects on WO_3 for photocatalytic CO_2-to-CH_4 conversion by water. *Proc. Natl. Acad. Sci. USA.* **121**, e2319751121 (2024).
40. Wang, J. et al. Visible-near infrared independent modulation of hexagonal WO_3 induced by ionic insertion sequence and cavity characteristics. *Adv. Mater.* **36**, 2406939 (2024).
41. Jiang, Y. et al. Electron ptychography of 2D materials to deep sub-ångström resolution. *Nature* **559**, 343–349 (2018).
42. Chen, Z. et al. Electron ptychography achieves atomic-resolution limits set by lattice vibrations. *Science* **372**, 826–831 (2021).
43. Zhang, Y. et al. Artificially controlled nanoscale chemical reduction in VO_2 through electron beam illumination. *Nat. Commun.* **14**, 4012 (2023).
44. Sha, H. et al. Deep sub-angstrom resolution imaging by electron ptychography with misorientation correction. *Sci. Adv.* **8**, eabn2275 (2022).
45. Yu, R. et al. Introduction to electron ptychography for materials scientists. *Microstructures* **4**, 2024056 (2024).
46. Sha, H. et al. Ptychographic measurements of varying size and shape along zeolite channels. *Sci. Adv.* **9**, eadf1151 (2023).
47. Cui, J. et al. Antiferromagnetic imaging via ptychographic phase retrieval. *Sci. Bull.* **69**, 466–472 (2024).
48. Henkelman, G. et al. A climbing image nudged elastic band method for finding saddle points and minimum energy paths. *J. Chem. Phys.* **113**, 9901–9904 (2000).
49. Shen, M. et al. Engineering the Atomic Configurations of Surface-Active Sites for Retuning the Photoreduction CO_2 Selectivity. *ACS Catal* **14**, 15908–15915 (2024).
50. Kresse, G. et al. Efficient iterative schemes for ab initio total-energy calculations using a plane-wave basis set. *Phys. Rev. B* **54**, 11169 (1996).
51. Kresse, G. et al. Efficiency of ab-initio total energy calculations for metals and semiconductors using a plane-wave basis set. *Comput. Mater. Sci.* **6**, 15–50 (1996).
52. Perdew, J. P. et al. Generalized gradient approximation made simple. *Phys. Rev. Lett.* **77**, 3865 (1996).
53. Perdew, J. P. et al. Rationale for mixing exact exchange with density functional approximations. *J. Chem. Phys.* **105**, 9982–9985 (1996).
54. Grimme, S. et al. A consistent and accurate ab initio parametrization of density functional dispersion correction (DFT-D) for the 94 elements H-Pu. *J. Chem. Phys.* **132**, 154104 (2010).
55. Monkhorst, H. J. et al. Special points for Brillouin-zone integrations. *Phys. Rev. B* **13**, 5188–5192 (1976).

Acknowledgements

W.X., Z.Y., R.Y., and S.X. acknowledge the support received from the National Natural Science Foundation of China (52222102, 52201006, 52388201, 22272024, and 22402033), Fund of Key Laboratory of Advanced Materials of Ministry of Education (53220330123), China Postdoctoral Science Foundation Funded Project (2024M750472) and Postdoctoral Fellowship Program of China Postdoctoral Science Foundation (GZC20230457). The authors acknowledge Beijing PARATERA Tech Co., Ltd. for providing access to high-performance computing resources.

Author contributions

W.X., S.X., Z.Y., and R.Y. conceptualized and designed the experiments. S.X. prepared the WO_3 samples with different thicknesses, executed the electrochromic experiments, and explored the reaction mechanism. J.C., W.X., and R.Y. conducted electron ptychography reconstructions. C.Z. carried out the electrochemical properties for WO_3 nanosheets and WO_3 nanosheets. M.S., X.L., Q.Z., and K.X. conducted an AC-STEM crystallography analysis. M.W., Y.Z., and W.X. constructed the atomic structures of the WO_3 materials and performed theoretical calculations. Y.Y. carried out the SEM characterization. C.Y. offered experiment recommendations. R. J. and R. W. performed the in-situ optical transmittance experiments. S.X., W.X., and R.Y. prepared and revised the manuscript. All authors have approved the final version of the manuscript.

Competing interests

The authors declare no competing interests.

Additional information

Supplementary information The online version contains supplementary material available at https://doi.org/10.1038/s41467-025-68046-z.

Correspondence and requests for materials should be addressed to Zhiyang Yu, Rong Yu or Wandong Xing.

Peer review information *Nature Communications* thanks Rudra Banerjee, Guofa Cai, and the other, anonymous, reviewer(s) for their contribution to the peer review of this work. A peer review file is available.